Characterisation of Smart CFRP Composites with Embedded PZT Transducers for Nonlinear Ultrasonic Applications

Christos Andreades [a], Pooya Mahmoodi [b], Francesco Ciampa [a,*]

[a] Materials and Structures Centre (MAST), Department of Mechanical Engineering, University of Bath, Bath, BA2 7AY, UK.

[b] Engineering Central (Innovation Hub), Swansea University Bay Campus, Fabian Way, Crymlyn Burrows Swansea, SA1 8EN, UK.

*Corresponding Author

E-mail address: f.ciampa@bath.ac.uk

ABSTRACT

Embedded piezoelectric lead zirconate titanate (PZT) transducers in carbon fibre reinforced plastic (CFRP) composites are typically electrically insulated by interlaying materials such as polyimide Kapton films between the PZT and the laminate ply. However, the presence of polymeric films may cause debonding at the layer interface and an increase of material distortion around the PZT, thus reducing the structural performance. This paper proposes an alternative insulation technique in which PZTs are covered by a thin layer of woven E-glass fibre fabric for enhanced adhesion with the surrounding epoxy matrix. An analysis of variance on experimental test results showed that the compressive, flexural and interlaminar shear strengths of plain CFRP specimens were equal to the means of the smart CFRP composite ($0.41<p<0.58$), but significantly higher from the means of Kapton specimens ($0.0001<p<0.05$). Thus, the proposed insulation technique had no impact on the mechanical properties of the laminate. Moreover, a post-test fractographic analysis indicated that at least one damage parameter (damage opening) in Kapton specimens was significantly larger (p=0.03) than in plain specimens, but the damage length and opening in the proposed woven E-glass fibre samples were equal to those in plain composites. Also, the brooming failure under compression was the same for the smart CFRP composite and the plain samples, whereas the Kapton specimens failed by through-thickness shear. Finally, nonlinear ultrasonic experiments were conducted on CFRP laminates with

artificial in-plane delamination using glass fibre insulated PZTs. The effect of second harmonic generation was found to be nearly two times higher than conventionally surface-bonded PZTs.

Keywords: Smart Structures; Composite Materials; Embedded Transducers; Structural health Monitoring; Nonlinear Ultrasound

1 INTRODUCTION

With growing demand from aerospace industry for next-generation lightweight, safe and technologically advanced structures, there is a strong need to develop fibre reinforced plastic (FRP) composites with integrated sensing capabilities. Surface-mounted piezoelectric lead zirconate titanate (PZT) transducers are typically used to sense the monitored component and provide real-time information about structural health conditions. PZT sensors have balanced actuation and sensing constants, as well as good thermal stability and resistance to high temperatures [1]. PZTs are able to convert changes in strain, pressure, force and acceleration into electrical signals, based on the piezoelectric effect [2]. The signals can then be processed with dedicated ultrasonic algorithms to provide information about the health status of components. However, the external exposure of PZTs to the surrounding environment (e.g. moisture and corrosion) makes them susceptible to failure [3]. Protection systems of externally mounted PZTs would dramatically increase manufacturing costs and weight. Hence, in order to improve the efficiency of smart composites with sensing features, PZT transducers have been inserted into layers of both glass and carbon fibre reinforced plastic (GFRP and CFRP) laminates [4]-[11]. The use of embedded PZT sensors has, therefore, led to the development of smart composites for ultrasonic structural health monitoring (SHM) applications.

However, one of the biggest challenges in the development of smart CFRP laminates is the need for insulation of embedded PZTs from electrically conductive carbon fibres. According to the literature, polyimide (Kapton) film is commonly used as an interlayer material between the sensor and the laminate plies due to its high temperature resistance [4]-[9]. A number of studies such as those by Mall

and Coleman [4], Paget and Levin [5] and Arellano et al. [3] proved that the tensile and compressive strength as well as the fatigue endurance of CFRP laminates were negligibly affected by the embodiment of PZTs insulated by Kapton film layers. However, to the best of authors' knowledge, only few studies analysed both flexural and interlaminar properties of smart composites with embedded PZT insulated by polymer layers. Lin and Chang [7], for example, investigated the interlaminar behaviour of their SMART Layer inserted into the laminate of a CFRP composite. Double lap shear and short beam shear tests revealed that the interlaminar properties of the CFRP laminate were not significantly affected by the presence of an additional phase within the composite. Nevertheless, it is well known that polymeric films made of Kapton and Teflon are typically used during the manufacturing process to generate controlled "artificial" delamination in composites [12]. Indeed, the presence of polymeric films within the laminate causes poor adhesion and debonding between plies, thus weakening the whole composite structure and creating interlaminar stresses surrounding the PZT sensor [13]. These stresses may even dramatically reduce the sensing ability of embedded transducers. Hence there is a need for alternative materials and processes to insulate embedded PZTs in CFRP composites.

This study proposes a novel material processing technique for the electrical insulation of circular PZTs inserted between the plies of CFRP laminates. In particular, a thin layer of woven E-glass fibre fabric was placed over the top (conductive) surface of the embedded PZT transducer, as illustrated in Figure 1. This novel smart composite was inspired from CFRP-Aluminium hybrid (CARALL) laminates in which glass fibres were integrated between the two materials to avoid corrosive degradation of surfaces [14]. The effect of the proposed embedding technique on the mechanical properties of the laminate was experimentally studied and compared with the effect of the conventional embedding technique using Kapton layers. This study was supported by a numerical finite element (FE) model, which was developed to provide initial information about the optimal position of the PZT and glass fibre along the thickness of the CFRP composite. The interlaminar shear strength, the flexural strength and compressive strength of CFRP laminates with embedded PZTs and a layer of woven E-glass fabric

(G-specimens) were determined by performing short-beam and long-beam three-point bending tests, and compression tests. The same tests were performed using plain CFRP laminates (P-specimens) as well as CFRP composites in which the embedded PZTs were covered by a 500HN Kapton film layer (K-specimens). In addition, all specimens were subject to post-test fractographic inspection with optical microscope to study the failure mode in each case study. Finally, the functionality of the proposed smart composite and its sensitivity in detecting material damage were examined by conducting Nonlinear Elastic Wave Spectroscopy (NEWS) experiments on CFRP plates with artificial in-plane delaminations.

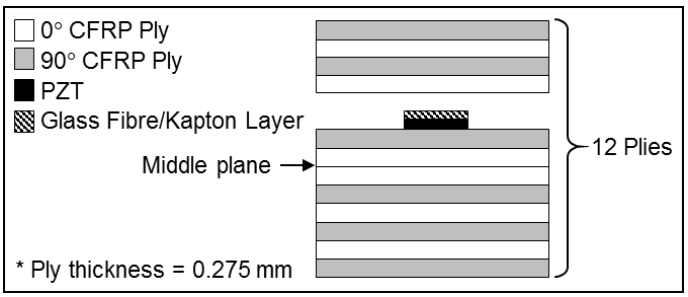

Figure 1: Configuration of embedded PZTs in CFRP laminates.

2 NONLINEAR ELASTIC WAVE SPECTROSCOPY METHODS

Over the years, a number of ultrasonic algorithms have been developed to detect material damage in CFRP laminates [15]-[17]. NEWS techniques have been widely used in composites due to their higher sensitivity over linear ultrasonic methods to detect damage at early stages of formation (e.g. micro-cracks, delamination and voids) [19]-[23]. In particular, elastic waves propagating through the material can force micro-crack interfaces to either oscillate ("clapping" motion) or move relative to each other ("rubbing" motion), thus resulting in the generation of nonlinear elastic effects such as higher harmonics (even and odd multiples) and sub-harmonics (sub-multiples) of ultrasonic excitation signals [24]. According to Landau and Lifshitz [25], in the "classical" nonlinear material response, second harmonic generation can be considered as the principal signature for damage identification. As reported by many authors (e.g. Landau and Lifshitz [25] and, more recently, Zargai et al. [26]), the one-dimensional elastodynamic wave equation in the second order approximation shows that the

displacement u of propagating elastic waves is not only dependent on the linear properties of the medium such as the speed of sound c_0, but also on the nonlinear parameter β:

$$\frac{\partial^2 u}{\partial t^2} - {c_0}^2 \cdot \frac{\partial^2 u}{\partial x^2} = -2\beta \cdot {c_0}^2 \cdot \frac{\partial u}{\partial x} \cdot \frac{\partial^2 u}{\partial x^2}. \quad (1)$$

This β parameter describes the second order nonlinear effect exhibited by the damaged material [26]. By measuring the signal amplitude at the fundamental and second harmonic frequencies (A_1 and A_2), the parameter β can be determined based on the following equation:

$$|\beta| = \frac{A_2}{{A_1}^2} \cdot \frac{4{c_0}^2}{x\omega^2}, \quad (2)$$

where x and ω are the propagation distance inside the material and the angular frequency of the input waveform, respectively. Since c_0, x and ω are constants, the parameter β can be easily considered as [26]

$$|\beta| \propto \frac{A_2}{{A_1}^2}. \quad (3)$$

It has been proved that the parameter β increases proportionally with material degradation [27] and its estimation, originally introduced by Buck et al. [28] and Antonets et al. [29], allows NEWS technique detecting damage in composites. Polimeno et al. [20] monitored the nonlinear response of a CFRP laminate with micro-cracks and delamination using a piezoelectric exciter and a microphone mounted onto the surface of the laminate. By exciting the laminate at one of its resonance frequencies and by monitoring the amplitude of harmonics in the spectrum of the received signal, second harmonic generation was proved to be highly accurate in the detection of damage and the estimation of damage size. More recently, Ciampa et al. [22] demonstrated that high order bispectral analysis of waveforms obtained using a pair of PZTs bonded onto the surface of a CFRP laminate with artificial delamination (i.e. Teflon insert) allowed the evaluation of second order nonlinearity. The “non-classical” nonlinear material response [30] including the effect of nonlinear local damage resonance (LDR) was also studied to enhance the identification of nonlinear elastic features in damaged materials [31]. In particular, if the driving frequency matches the damage resonance frequency, the vibrational amplitude of

nonlinear elastic effects can be dramatically increased (up to ~20-40 dB). This LDR effect leads to a very efficient energy pumping at the damage area and ensures that even a low input acoustic power of few mW is sufficient to generate nonlinear elastic effects at the crack location. As a result, superharmonics of the LDR frequency in addition to higher harmonics of the input frequency can be generated [23]. This effect was analytically demonstrated by Solodov et al. [32] using a 1D model of a linear damped oscillator. Ciampa et al. [23] not only validated the results from the study of Solodov, but also introduced a 2D mathematical model and proved theoretically and experimentally the existence of intermodulation effects of the LDR frequency. However, the vast majority of NEWS testing has been performed using surface-bonded PZTs [18]-[23]. Sensor embedment would offer, instead, the opportunity to achieve better coupling with the material, thus resulting in higher signal amplitude and enhanced sensitivity for damage detection [33].

3 ASSESSMENT OF MECHANICAL PROPERTIES

This section outlines the numerical and experimental work performed to analyse the combined effect of the embedded PZT and its insulating layer on the mechanical properties of CFRP laminates.

3.1 Numerical Finite Element Models

Prior to the specimen manufacture, static short-beam tests were simulated with FE models using ANSYS Workbench software (in accordance with the BS-EN-ISO-14130:1997 standard [34]). The aim of the numerical simulations was to determine the optimal position of the PZT and glass fibre along the thickness of the CFRP composite subject to three point bending, which minimised the interlaminar shear effects in the laminate. A standard cross-ply stacking sequence of the CFRP composite, which is widely used in aerospace applications (Figure 1), was here selected and employed in the numerical models and in the experimental Section 3.3. The CFRP and glass fibre layers, the PZT, the loading head and the supports were simulated using 3D 20-noded SOLID186 elements. This element type offers mixed formulation capability for simulating deformations of nearly incompressible elastoplastic

materials. The loading head and supports were modelled as rigid hollow cylinders. The total number of elements was 67,860. Similarly to Moulin et al. [35], the epoxy resin-rich regions (Figure 2b) formed at the periphery of the PZT and the glass fibre layer were modelled as pure resin. Whilst the CFRP composite lamina and the glass fibre layer were assumed to be homogenous and transversely isotropic, the resin and PZT sensor were considered as homogenous and isotropic. The elastic properties of all materials including the Young's modulus, E, the shear modulus, G and the Poisson's ratio, ν, along with tensile, compressive and shear strengths (X, Y and S) are provided in Tables 1 and 2. The subscripts 1 and 2 in each elastic constant denote the longitudinal and the transverse direction in the plane of the lamina, whilst 3 is the thickness direction. A cohesive zone model (CZM) represented by 3D 16-noded INTER204 elements was introduced at layer-layer and layer-PZT interfaces. Generally, INTER204 elements can simulate an interface between two surfaces and the subsequent delamination process, when used with SOLID186 elements. In addition, the frictionless Hertzian contact model represented by element types CONTA174 and TARGE170 was used to simulate the contact between the loading head and the laminate and between the laminate and supports. Typically, CONTA174 elements are located on SOLID186 surfaces, and TARGE170 overlay the SOLID186 elements.

Table 1: Properties of CFRP layer and woven E-glass fibre fabric layer.

Orthotropic Property	**CFRP Layer [36],[37]**	**Woven E-glass Fibre Fabric Layer [38], [39]**
E_1, E_2, E_3 (GPa)	172, 8.9, 8.9	12.5, 11.8, 11.8
G_{12}, G_{13}, G_{23} (GPa)	4.2, 4.2, 0.0225	3.5, 3.5, 3.5
v_{12}, v_{13}, v_{23}	0.35, 0.35, 0.01	0.17, 0.17, 0.07
X_1, X_2 (MPa)	2200, 61	322, 290
Y_1, Y_2 (MPa)	2200, 130	204, 200
S_1, S_2 (MPa)	85, 40	39, 39

Table 2: Properties of PZT and resin.

Isotropic Property	**PZT [40]**	**Resin [41]**
E (MPa)	1.1E+05	3780
G (MPa)	4.1E+04	1400
v	0.34	0.35
X (MPa)	290	54.6

Three FE models of the CFRP laminate with embedded PZT and glass fibre located at different depths along the thickness were created. In the first FE simulation, the PZT and glass fibre were inserted at the middle plane, i.e. between layers 6 and 7 from the bottom (see Figure 1). In the second and third FE models, the PZT and glass fibre were inserted towards the laminate region under compression (between layers 8 and 9) and tension (between layers 4 and 5), respectively. As illustrated in Figure 2a, the PZT was not placed midway along the specimen length to avoid compressing it directly with the loading head. In this numerical analysis, it was assumed that boundary conditions remained constant during loading and that the CFRP material was deformed within their elastic region. Simulations were performed by applying a static nodal displacement of 0.4 mm to the loading head with a direction perpendicular to the laminate surface. Moreover, perfect bonding between the PZT, the glass fibre layer and CFRP layers was assumed.

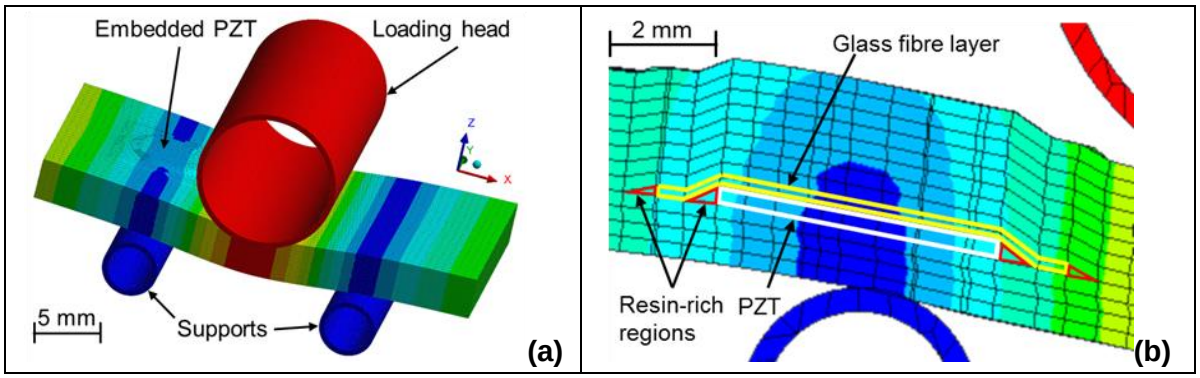

Figure 2: Illustration of the geometry used for the numerical FE short beam three point bending test (a) and a zoom of the section view of the numerical model with the PZT inserted between layers 4 & 5 (b).

The ANSYS's built-in Hashin's model for damage initiation and evolution was here used to identify the regions within the sample at which tensile or compressive damage in the fibre and matrix was initiated. This is described by the following four failure criteria modes for damage initiation [42]

Fibre Tension ($\hat{\sigma}_{11} \geq 0$) : $$F_f^t = \left(\frac{\hat{\sigma}_{11}}{X_1}\right)^2 + \left(\frac{\hat{\tau}_{12}}{S_1}\right)^2; \quad (4)$$

Fibre Compression ($\hat{\sigma}_{11} < 0$): $$F_f^c = \left(\frac{\hat{\sigma}_{11}}{Y_1}\right)^2; \quad (5)$$

Matrix Tension ($\hat{\sigma}_{22} \geq 0$): $$F_m^t = \left(\frac{\hat{\sigma}_{22}}{X_2}\right)^2 + \left(\frac{\hat{\tau}_{12}}{S_1}\right)^2; \quad (6)$$

Matrix Compression ($\hat{\sigma}_{22} < 0$): $$F_m^c = \left(\frac{\hat{\sigma}_{22}}{2S_2}\right)^2 + \left[\left(\frac{Y_2}{2S_2}\right)^2 - 1\right]\frac{\hat{\sigma}_{22}}{Y_2} + \left(\frac{\hat{\tau}_{12}}{S_1}\right)^2; \quad (7)$$

where $\hat{\sigma}_{ij}$ and $\hat{\tau}_{ij}$ are the normal and shear components of the effective stress tensor, respectively. The constitutive law is provided by the following equation [36]

$$\sigma = C_d \varepsilon, \tag{8}$$

where σ is the true stress converted into the effective stress $\hat{\sigma}$ through a tensor operation [36], ε is the true strain and C_d is the damage elasticity matrix which describes material damage and has the following form

$$C_d = \frac{1}{D}\begin{bmatrix} (1-d_f)E_1 & (1-d_f)(1-d_m)\nu_{21}E_1 & 0 \\ (1-d_f)(1-d_m)\nu_{12}E_2 & (1-d_m)E_2 & 0 \\ 0 & 0 & D(1-d_s)G_{12} \end{bmatrix}, \tag{9}$$

where d_f, d_m and d_s are damage variables for tension, compression and shear [36], and

$$D = 1 - \big(1-d_f\big)(1-d_m)\nu_{12}\nu_{21} > 0. \tag{10}$$

Once the four failure criteria modes for damage initiation (4 - 7) are satisfied, further loading will cause a variation of the coefficients of the damage elasticity matrix (9) as function of damage variables d_i [36]. Indeed, the effective stress is equal to the true stress only if damage is not initiated, since damage variables are initially set equal to zero. An in-built damage evolution law for the damage variable in ANSYS is used to simulate the in-ply damage in each lamina. The damage evolution law is known as Continuum Damage Mechanics method that models gradually increasing damage. This is defined in terms of the fracture energy dissipated during the damage process, which is a generalization of the CZM using cohesive elements [42], [43]. The input parameter is the energy dissipated per unit area G^C that accounts for fibre tension G_{ft}^C, fibre compression G_{fc}^C, matrix tension G_{mt}^C and matrix compression G_{mc}^C. Values used in this model of the energy dissipated for the CFRP material have been taken from literature and are equal to $G_{ft}^C = G_{fc}^C = 70$ mJ/mm^2 and $G_{ft}^C = G_{fc}^C = 0.25$ mJ/mm^2 [36]. As a result of the damage evolution law, an equivalent damage index variable *d* is obtained, which ranges from zero (undamaged material) to one (fully damaged material) and accounts for all four above mentioned different modes. As illustrated in Figure 3 and Figure 4, damage was analysed at two specific layers in

each FE simulation. For clarity, Figure 4 is an enlargement of Figure 3. The first layer examined was the CFRP ply under the PZT and glass fibre (Figure 3). Numerical results suggested that the centre of this layer (under the loading head) was more prone to fibre failure whereas, near the PZT periphery, delamination was more likely to occur. The second layer under examination was the glass fibre layer on top of the PZT (Figure 4). Also here, failure results revealed that damage was more likely to occur at the PZT periphery in the form of delamination. Although these observations were common between the three FE simulations, the lowest damage variable values (from 0 to 1) were obtained with the PZT and glass fibre layer placed above the middle plane. Conversely, the highest values were obtained with the PZT and glass fibre layer placed exactly at the middle plane. Failure results of FE simulations are summarised in Table 3. Based on this analysis, the PZT position with the minimum effect on the structural integrity of the laminate was achieved towards the surface under compression (i.e. between layers 8 and 9). Therefore, this final lay-up and PZT position (see Figure 1) were chosen for all specimens used in the experimental mechanical tests.

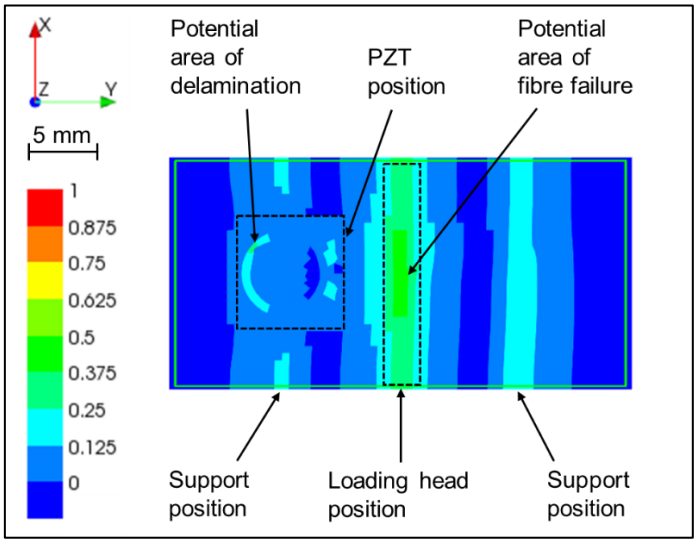

Figure 3: Contour plot of Hashin's damage index values on the CFRP Layer under the PZT (top view). The PZT and glass fibre layer were inserted between layers 8 & 9.

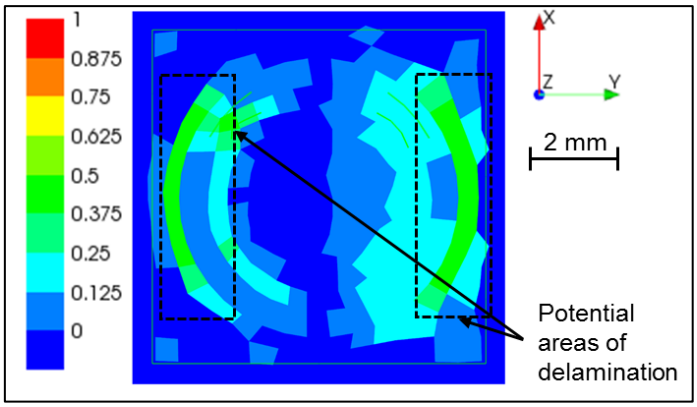

Figure 4: Contour plot of Hashin's damage index values on the glass fibre layer above the PZT (top view). The PZT and glass fibre layer were inserted between layers 8 & 9.

Table 3: Summary of Hashin's Failure Values.

PZT Position	**Maximum Damage Index Value**		
	CFRP Layer (at middle)	CFRP Layer (at PZT periphery)	Glass Fibre Layer (at PZT periphery)
Between layers 4 & 5	0.776	< 0.750	0.956
Between layers 6 & 7	0.663	< 0.500	0.774
Between layers 8 & 9	0.546	< 0.375	0.607

3.2 Specimen Manufacture

Three groups of six CFRP specimens (six P-, six G- and six K-specimens) were manufactured for each test (bending and compression). One specimen from each group was kept in pristine condition (control specimens) and used in post-test fractographic comparisons with damaged specimens. All samples were cut from larger plates (using a water-cooled diamond saw) made from unidirectional carbon/epoxy prepregs (Hexcel T800/M21) in [90°/0°/90°/0°/90°/0°]s stacking sequence, with a total thickness of around 3 mm (Figure 1). The composite plates were originally laid up by hand and cured inside an autoclave for 120 minutes at a pressure of 0.7 MPa and a temperature of 180^{o}C with a ramp rate of 3^{o}C/min. The diameter of the PZT was 6 mm and its thickness 0.3 mm. In G- and K-specimens, the size of glass fibre/Kapton layer over the PZT was approximately 10 x 10 mm.

3.2.1 Specimens used in Short-Beam and Long-Beam Bending Tests

The specimens used in the short-beam and the long-beam bending tests were manufactured in accordance with Section 3.1 and the BS EN ISO 14130:1997 and ASTM D7264/D7264M-07 standards, respectively [34], [44]. The dimensions of both specimen types are shown in Figure 5.

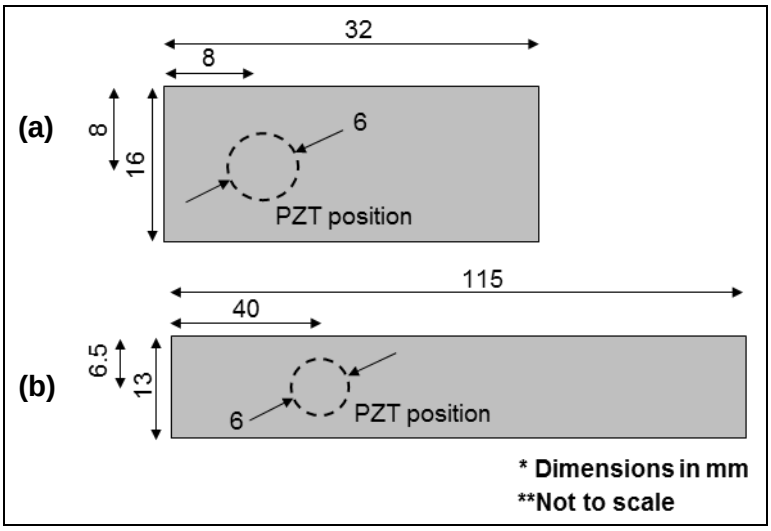

Figure 5: Dimensions of short-beam specimens (a) and long-beam specimens (b) used in bending tests.

3.2.2 Specimens used in Compression Test

The specimens used in the compression test were manufactured in accordance with Section 3.1 and BS-EN-ISO-14126:1999 standard [45]. As shown in [46], the ends of the specimens were reinforced using tabs on either side to avoid damaging of the specimen during testing. For this reason, the PZTs were placed midway along the un-tabbed length of the specimens. The tabs were cut from larger plates made from unidirectional glass/epoxy prepregs (Hexcel UD192/8552). These were laid up by hand in [90°/0°/90°/0°/90°/0°]s stacking sequence and cured under the same conditions as the CFRP plates (ref. 3.2) but for 60 minutes longer. The tab plates were adhered to the CFRP plates before cutting of individual specimens using a two-part epoxy adhesive (Araldite 420 A/B) and the assembly was cured in accordance with the test standard.

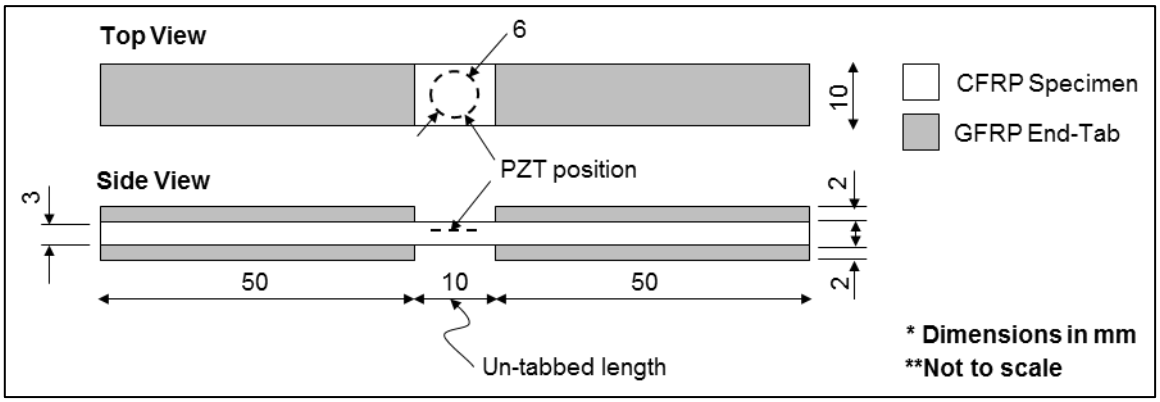

Figure 6: Dimensions of specimens used in compression tests.

3.3 Experimental Mechanical Tests

3.3.1 Short-Beam and Long-Beam Three-Point Bending Tests

The two mechanical tests were performed using a three-point bending configuration (Figure 7). According to the BS EN ISO 14130:1997 standard, the short-beam test was performed by maintaining a span-to thickness ratio of 5:1 and using a loading roller and supporting rollers of 5mm and 2mm radii respectively. In the long-beam test, the span-to-thickness ratio was 32:1 and all three rollers had a radius of 3mm in agreement with the ASTM D7264/D7264M-07 standard. All CFRP samples in both tests were loaded to failure on an Instron machine (Tabletop Model 3369) after setting the velocity of the loading head to 1 mm/min.

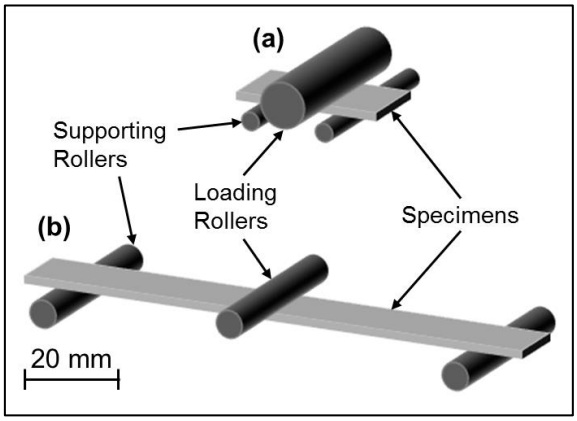

Figure 7: Schematic of short-beam (a) and long-beam (b) three-point-bending configurations.

3.3.2 Compression Test

According to method 1 of BS-EN-ISO-14126:1999 standard, the compressive load was applied to the specimens by shear through the surfaces of the end-tabs. A schematic of the compression fixture used is depicted in Figure 8. Briefly, each specimen was symmetrically clamped inside the fixture with its end-tabs being held between two rectangular steel blocks using eight bolts. A 10 mm gap was maintained between the top and bottom blocks; equal to the un-tabbed length of the specimen. The CFRP samples were compressed to failure on an Instron machine (Floor Model 5585) using a loading head velocity of 1 mm/min. The load was applied perpendicularly the top set of blocks that could move relative to the bottom blocks through the alignment rods.

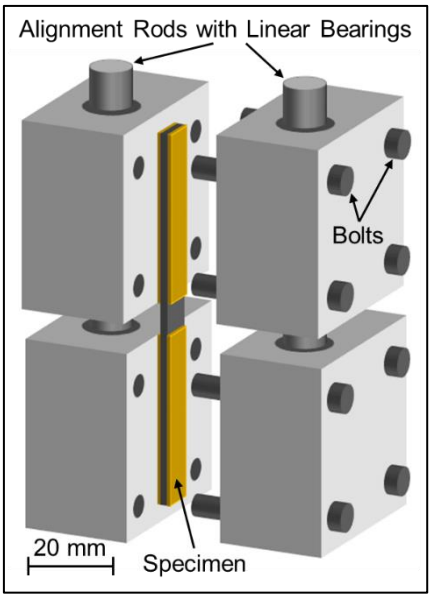

Figure 8: Schematic of compression test fixture.

3.4 Post-Test Fractographic Inspection of CFRP Specimens

After completing the tests, all short-beam and the long-beam specimens were encapsulated into epoxy resin to maintain their state of failure. Samples were then sectioned along their long axis to expose their internal structure (Figure 9). The failure mode and damage size in G- and K-specimens were studied and compared with those in P-specimens using a high-quality scanner (Epson Expression 1680 Professional) and an optical microscope (Leica DFC425). The control (pristine) specimens were also encapsulated into the epoxy resin and used for comparisons with damaged specimens. The failure

mode in compression samples was directly examined using the optical microscope. The failure mode in compression samples was directly examined with the optical microscope. Encapsulation into epoxy resin was not possible because, as expected, the failure was not uniform along samples' width.

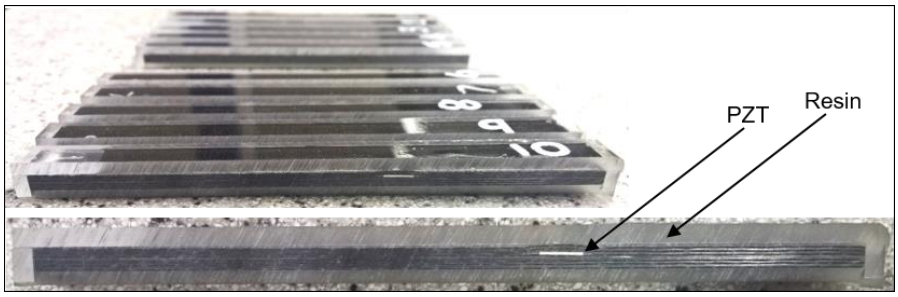

Figure 9: Long-beam specimen - section view.

3.5 Results and Discussion

A standard one-way analysis of variance (ANOVA) was conducted using Matlab to statistically determine if there was a significant difference initially between the group means of P- and G-specimens, and then between P- and K-specimens. The null hypothesis (H_0) was that the group means were equal and the alternative hypothesis (H_A) that the means were not equal, with a significance level (α) of 0.1 (i.e. 90% confidence level). Briefly, in one-way ANOVA the F-value (or F-statistic) is the following ratio [46]:

$$F = \frac{Variation\ Between\ Groups}{Variation\ Within\ Groups} \tag{11}$$

For a true null hypothesis, F-value should be approximately equal to 1 with the sampling fluctuations following an F distribution. The F distribution was characterised by the numerator degrees of freedom (df_N) and the denominator degrees of freedom (df_D), where df_N was equal to number of groups minus 1 (i.e. 2-1=1) and the df_D was equal to the total group data minus the number of groups (i.e. 10-2=8) [47]. The probability (p-value) that F-value would exceed the computed test-statistic was derived by ANOVA from the cumulative distribution function of F distribution [48]. For p-values smaller than α (p < 0.1) the null hypothesis was rejected meaning that the group means were significantly different. Inversely, for p > 0.1 the null hypothesis was accepted.

3.5.1 Mechanical Testing Results

3.5.1.1 Short-Beam and Long-Beam Three-Point Bending Tests

The results from the two bending tests along with the F- and p-values form ANOVA are presented in Table 4. In the short-beam bending test, P- and G-specimens failed on average at a maximum interlaminar shear stress of around 51 MPa and a maximum deflection of 0.81 mm. The ANOVA results verified that the means of interlaminar shear strength and maximum deflection between these two groups were equal; p=0.45 and p=0.41 respectively. On the other hand, K-specimens failed on average at a maximum interlaminar shear stress of 45.6 MPa and a maximum deflection of 0.76 mm which were found to be significantly lower (p=0.0001 and p=0.0014) than the values of P-specimens.

With regards to the long-beam bending test, the mean values of maximum flexural stress and maximum deflection of the P- and G-specimens were around 735 MPa and 8.56 mm, without any significant difference (p=0.47 and p=0.53). The corresponding values for the K-specimens were 685.7 MPa and 8.07 mm which were confirmed to be significantly different from those of P-specimens (p=0.01 and p=0.05).

3.5.1.2 Compression Test

Similarly, the compression test results (Table 4) indicated that the average compressive strength and maximum compressive extension of P- and G-Specimens were almost the same (p=0.46 and p=0.58) and around 495 MPa and 1.035 mm. Again, for p-values of 0.0023 and 0.032, the mean compressive strength (438.9 MPa) and extension (0.95 mm) of K-specimens were evidently lower compared with P-specimens.

Table 4: Summary of mechanical testing results.

Test	Property	P Specimens	G Specimens	K Specimens
Short-Beam Bending	**Int. Sh. Strength (MPa)** [a]	**51.0** (1.2)	**50.5** (1.0)	**45.6** (1.2)
	F-value	-	0.68	50.94
	p-value	-	0.4327	0.0001
	Max. Deflection (mm) [a]	**0.82** (0.02)	**0.80** (0.02)	**0.76** (0.02)
	F-value	-	0.78	22.6

	p-value	-	0.4106	0.0014
Long-Beam Bending	**Flex. Strength (MPa)** [a]	**741.3** (24.3)	**729.7** (24.6)	**685.7** (28.4)
	F-value	-	0.57	11.1
	p-value	-	0.4722	0.0104
	Max. Deflection (mm) [a]	**8.66** (0.42)	**8.46** (0.53)	**8.07** (0.41)
	F-value	-	0.44	5.08
	p-value	-	0.528	0.0542
Compression	**Comp. Strength (MPa)** [a]	**499.8** (21.1)	**488.8** (23.4)	**438.7** (22.9)
	F-value	-	0.61	19.18
	p-value	-	0.4579	0.0023
	Max. Comp. Ext. (mm) [a]	**1.05** (0.06)	**1.02** (0.08)	**0.95** (0.06)
	F-value	-	0.34	6.72
	p-value	-	0.5777	0.032

[a] Standard deviation in brackets

3.5.2 Fractography Results

3.5.2.1 Short-Beam Specimens

As depicted in Figure 10 and Figure 11, by observing the failure mode of short-beam specimens, interlaminar shear occurred at the interface between the two middle layers (6 and 7) and close to the specimen ends in all three types of specimen (P, G and K). In G-specimens the glass fibre layer over the PZT could not be easily visualised as it was covered by the matrix during the curing process. The propagation length (L) and opening (H) of shear damage were both measured in all specimens (Figure 11b) and the average values for each specimen group were calculated. The damage opening in each specimen was measured as the average of three measurements along the damage length (please see the experimental results in Table 5). The results from ANOVA suggested that the mean value of L in P-specimens was not different from that in G- and K-specimens (p=0.71 and p=0.37), but L was much more similar between P- and G-specimens rather than P- and K-specimens. On the other hand, the average value of H in P-specimens was found to be the same only with that in G-specimens (p=0.45), and significantly lower than in K-specimens (p=0.03). In addition, by examining the distribution of CFRP layers around the PZT, no difference was observed between the damaged and the control specimens within each specimen group. It must be noted that the splitting of CFRP layers up to few hundred

microns away from the PZT periphery (Figure 11c) was due to the direct insertion of the PZT and not to damage.

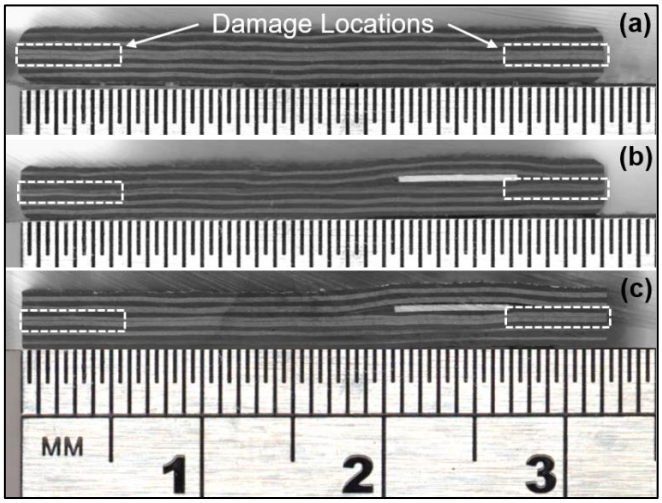

Figure 10: Short-beam specimens - cross-sectional view of damaged P-specimen (a), G-specimen (b) and K-specimen (c).

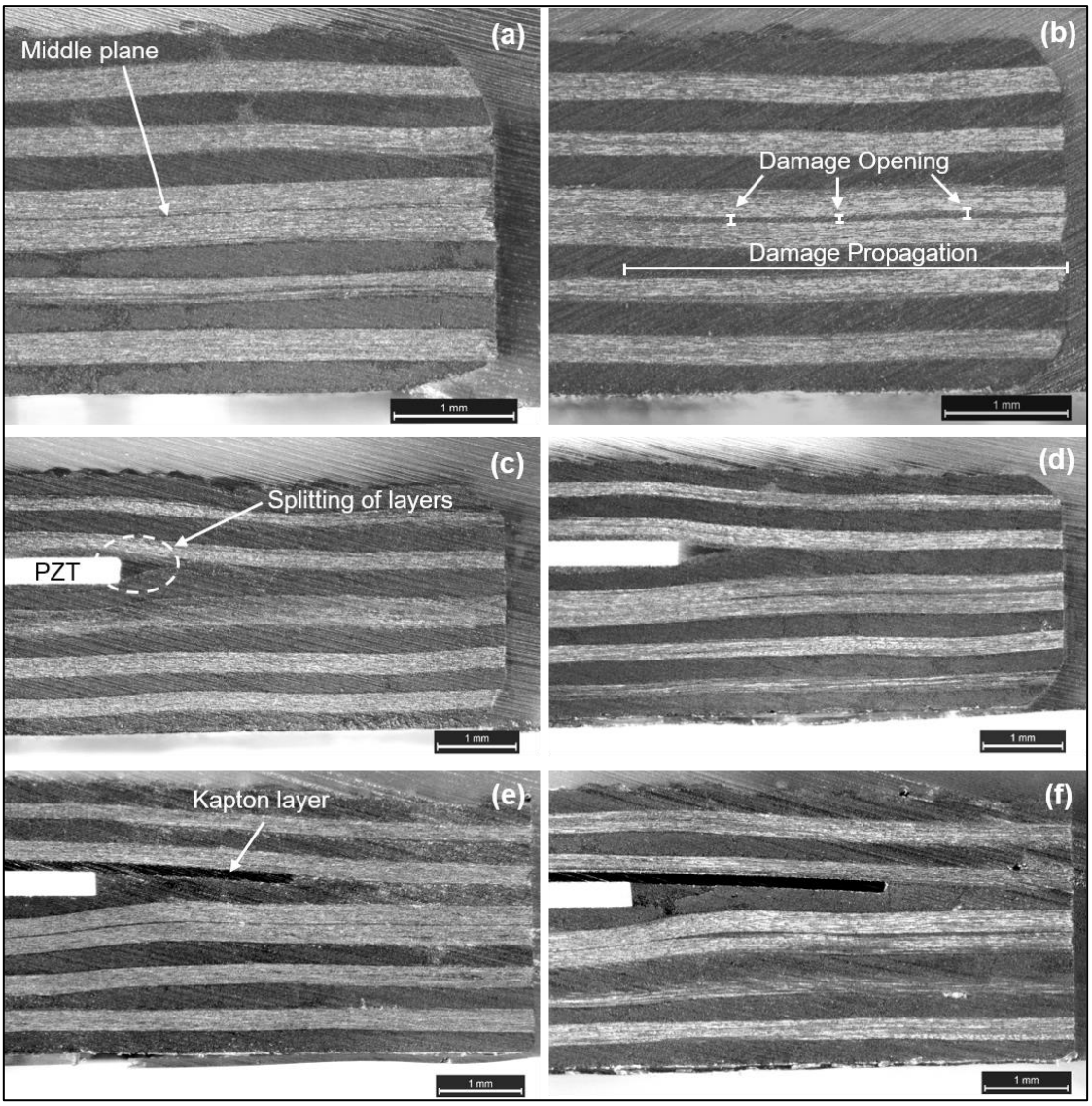

Figure 11: Short-beam specimens - closer view of specimen ends in the control P-specimen (a), damaged P-specimen (b), control G-specimen (c), damaged G-specimen (d), control K-specimen (e) and damaged K-specimen (f).

Table 5: Summary of damage measurements in short-beam specimens.

Damage Size	**P Specimens**	**G Specimens**	**K Specimens**
L (mm) [a]	**3.484** (0.477)	**3.599** (0.449)	**3.751** (0.413)
F-value	-	0.15	0.9
p-value	-	0.7050	0.3711
H (mm) [a]	**0.058** (0.022)	**0.061** (0.026)	**0.063** (0.024)
F-value	-	0.62	7.53
p-value	-	0.4541	0.0253

[a] Standard deviation in brackets

3.5.2.2 Long-Beam Specimens

With regards to the long-beam specimens used in the flexural test, the failure mode was also the same for all three specimen types. Damage occurred on the compression surface (top) midway along the specimen length as depicted in Figure 12. Closer inspection of the areas next to the damage and the PZT (Figure 13) revealed that fibre breakage occurred at the top three to five plies followed by in-plane delamination of the same plies up to few hundred microns away from the crack. By comparing the damaged specimens with the control specimens, no difference was noticed in the distribution of CFRP layers around the PZT. Similarly to the short-beam test, both L and H of delamination were here measured in all specimens (Figure 13), and the results are summarised in Table 6. The average values of L and H in both G- and K-specimens were considered equal to the values in P-specimens based on the ANOVA results (p > 0.1 in all cases). However, H and L values were again more similar between P- and G-specimens (p=0.87 and p=0.74) than between P- and K-specimens (p=0.79 and p=0.68).

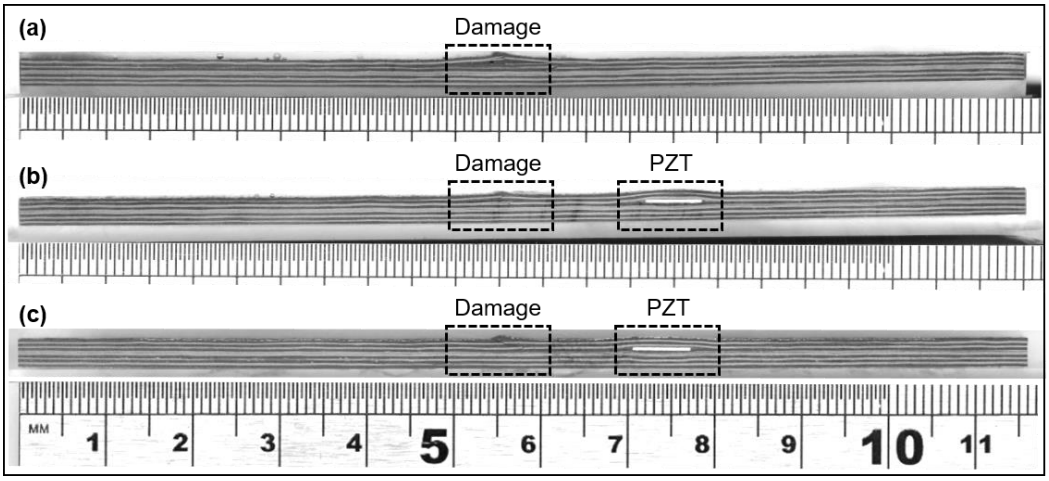

Figure 12: Long-beam specimens - cross-sectional view of P-specimen (a), G-specimen (b) and K-specimen (c).

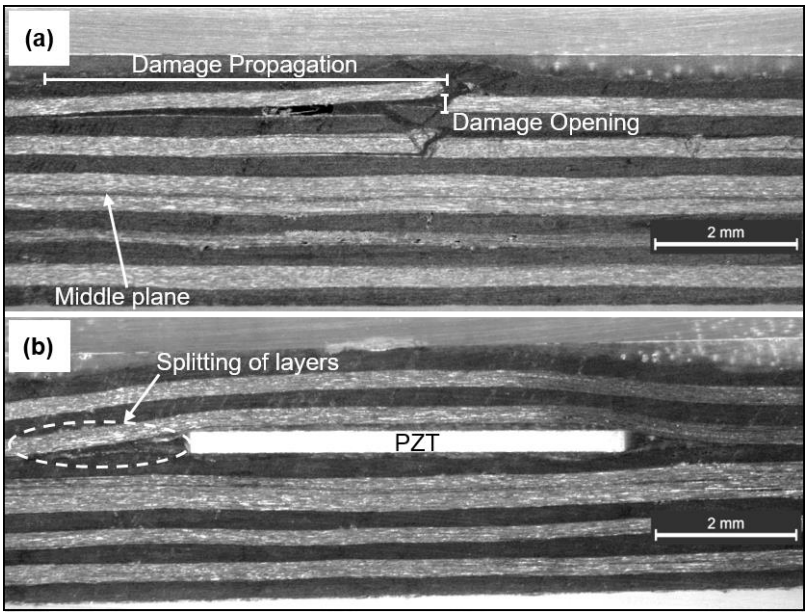

Figure 13: Long-beam specimens - closer view of damage area (a) and PZT area (b).

Table 6: Summary of damage measurements in long-beam specimens.

Damage Size	P Specimens	G Specimens	K Specimens
L (mm) [a]	**5.595** (1.556)	**5.742** (1.274)	**5.863** (1.462)
F-value	-	0.03	0.08
p-value	-	0.8745	0.7867
H (mm) [a]	**0.199** (0.030)	**0.206** (0.034)	**0.207** (0.027)
F-value	-	0.12	0.19
p-value	-	0.7398	0.6761

[a] Standard deviation in brackets

3.5.2.3 *Compression Specimens*

In the case of compression tests, damage in all P-, G- and K-specimens occurred within the un-tabbed section as expected. According to Figure 14, failure in K-samples was a combination of central through-thickness shear up to the plane of PZT/Kapton layer followed by complete delamination along that plane and finally through-thickness shear at both ends of un-tabbed section. G-samples also included a noticeable delamination at the plane of PZT/glass fibre layer. However, the brooming failure in both G- and P- specimens appeared to be almost identical.

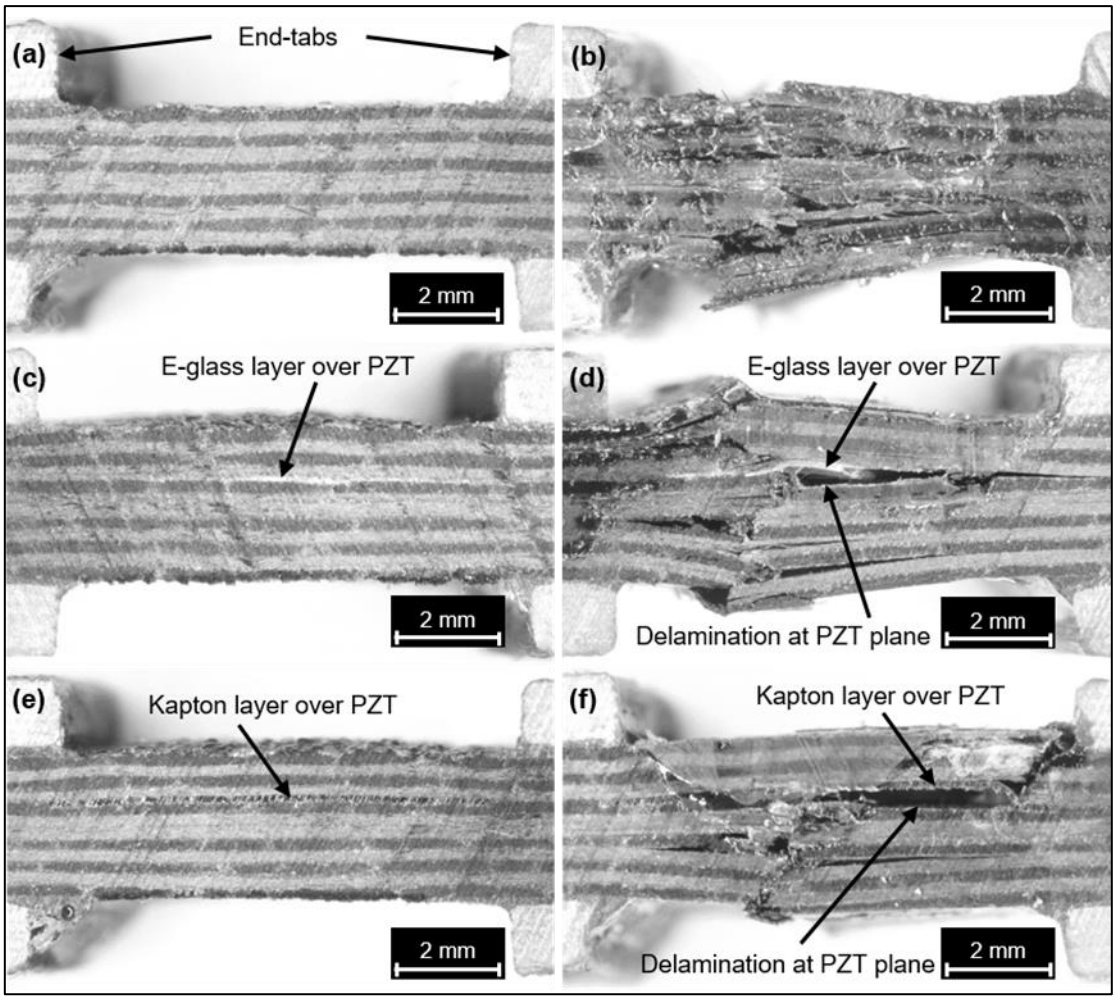

Figure 14: Compression specimens - closer view of un-tabbed section in the control P-specimen (a) damaged P-specimen (b), control G-specimen (c), damaged G-specimen (d), control K-specimen (e) and damaged K-specimen (f).

4 FUNCTIONALITY AND SENSITIVITY OF EMBEDDED TRANSDUCERS

Embedded PZTs with glass fibre layers were tested for the transmission and reception of elastic waves through the CFRP laminate in order to detect internal damage. The aim of this Section was (i) to prove the effectiveness of glass fibre layers in protecting PZTs from being short-circuited and (ii) to demonstrate the ability of detecting internal damage using embedded PZTs and nonlinear ultrasounds. The sensitivity of the embedded PZTs to material damage was also compared with the sensitivity of surface-bonded PZTs. A double patch made from Fluorinated Ethylene Propylene (FEP) release film (12μm thick) was inserted in CFRP laminates to generate controlled “artificial” in-plane delamination [12].

4.1 Specimen Manufacture

Three 120 x 30 mm CFRP specimens with [90°/0°/90°/0°/90°/0°]s lay-up were manufactured using the same process described in Section 3.2. Each specimen included a 10 x 10 mm double FEP patch at its centre, between layers 8 and 9 (from the bottom). As depicted in Figure 15, all specimens included a pair of PZTs. In specimen 1, the transmitter PZT was placed between the same layers as the patch whereas the receiver PZT between layers 4 and 5. In specimen 2, both PZTs were placed at the same level as the patch. Both specimens included a glass fibre layer over the sensor for the electrical insulation of each PZT. Finally, in specimen 3 both transducers were bonded to the material surface using a conventional super glue (Loctite GO2 gel). The propagation of elastic waves through the material was expected to excite and vibrate the debonded layers (under clapping and rubbing motion) associated with the LDR effect, thus leading to the generation of new waves that could be detected as higher harmonics of excitation signal. As previously mentioned, the second harmonic was here used as the elastic signature for damage detection [23], [25].

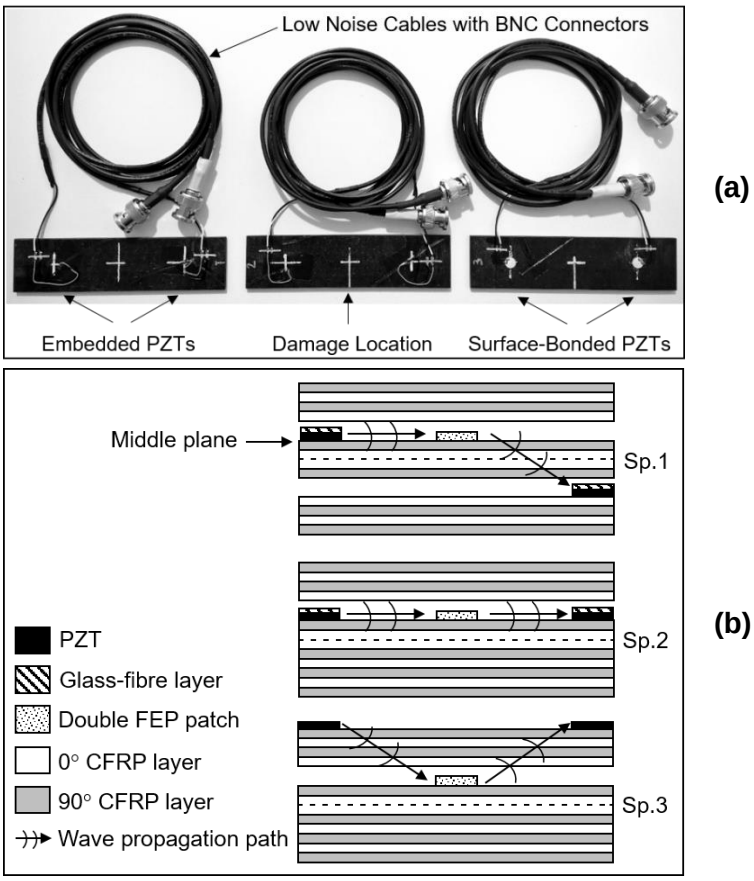

Figure 15: Composite specimens used in NEWS experiment with embedded transducers (a) and their lay-up (b).

4.2 Experimental Procedure

A continuous periodic signal generated from an arbitrary waveform generator (TTi TGA12104) was sent to the transmitter PZT through a voltage amplifier (Falco Systems WMA-300) with a 50x amplification factor. The receiver PZT was connected to an oscilloscope (PicoScope 4423) and both the time domain and the frequency domain of the received signals were monitored at a sampling frequency of 350 kHz with an acquisition time of 2 ms (Figure 16).

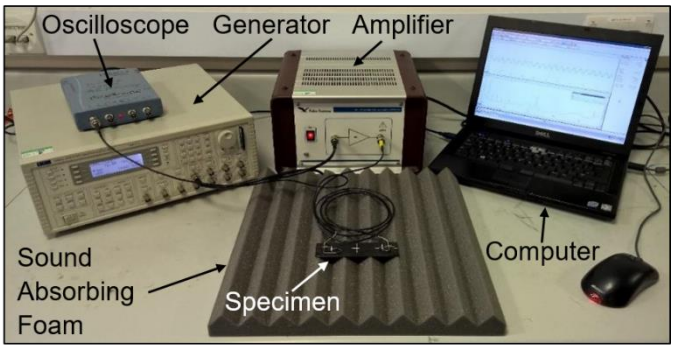

Figure 16: Illustration of set-up used in NEWS experiment.

Initially, a frequency sweep was performed to identify the input frequency associated with the crack. The LDR frequency was found to be at 15 kHz. Hence, to achieve higher excitation of the debonded layers (at the patch location), a continuous signal at the input frequency of 15 kHz was transmitted. Different input voltages at 75 V, 87.5 V, 100 V, 112.5 V and 125 V were here tested. The material response was scanned using a Laser Doppler Vibrometer in order to verify that the frequency of 15 kHz was indeed associated with the damage location (i.e. with location of the FEP patch). For an input PZT signal of 100 V at 15 kHz, the out-of-plane vibrational velocity at 30kHz (second harmonic of input frequency) was measured on the surface of specimen 1. A three-dimensional plot of the results around the patch area is presented in Figure 17a and Figure 17b, which reveal that the area at which the vibrational velocity was higher matched the position of the FEP patch. From Figure 17a and Figure 17b, it can also be seen that the higher harmonic second response (i.e. the red zone) was also similar to the size of the patch (around 10 x 10 mm). These measurements proved that second harmonic generation

caused by the LDR effect of the debonded layers occurred uniquely at the damage location and not elsewhere.

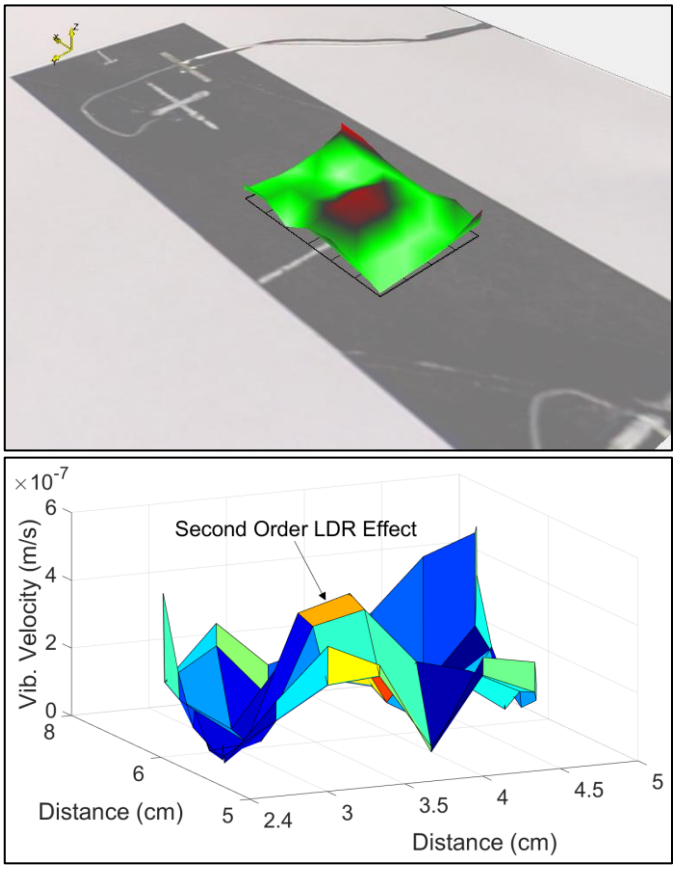

Figure 17: Illustration of the damaged area scanned by the laser Doppler vibrometer (a) and 3D representation of the out-of-plane vibrational velocity on the specimen 1 surface at the second harmonic frequency of 30 kHz.

4.3 Results and Discussion

The proposed technique for electrical insulation of the embedded PZTs with glass fibre layers was proved to be successful because the transmission and reception of signals was achieved in both specimens 1 and 2 without the formation of short-circuits. For the case of input signal of 100 V, the amplitude of the received signals in the time domain and the frequency domain are shown in Figure 18. The presence of A_2 harmonic verified that in-plane delamination in CFRP laminates could be detected using the proposed configuration of embedded PZTs. The amplitude at A_2 harmonic corresponding to the embedded PZTs (specimens 1 and 2) was an order of magnitude higher relative to that of surface bonded PZTs (specimen 3) indicating higher sensitivity in internal damage detection. This could be explained by considering the attenuation (energy loss) of the waves propagating through

each specimen. The propagation distance from the transmitter to the receiver PZT as well as the distance from the damage location to the receiver PZT was shorter in specimens 1 and 2 relative to specimen 3 Consequently, the attenuation of waves was lower in both specimens with embedded PZTs resulting in a higher A_2 amplitude.

For a more accurate comparison between the two specimens with embedded PZTs, the $\beta = A_2/A_1$^2 ratio was calculated using the results from the case of input signal of 100V (Table 7). As explained in Section 2, the parameter β is proportional to the material degradation. By assuming that the damage size was very similar in all specimens, any variation in parameter β between the specimens would indicate a variation in damage sensitivity. The configuration of PZTs in specimen 2 was found to be more sensitive to damage detection (β = 0.00065) relative to that in specimen 1 (β = 0.00042). This was reasonable based on the attenuation of waves explained above. The same ratio was also calculated for specimen 3. As it was expected, that was significantly lower (β = 0.00023) than the other two indicating that the surface-bonded PZTs were less sensitive to damage detection than the embedded PZTs. The observations described above were also valid for the remaining four cases of input voltage. In fact, by increasing the voltage from 75 V to 125 V, the signal amplitude of both the A_1 and the A_2 terms increased. In all cases, β was approximately two to three times higher for the embedded PZTs. Between specimens 1 and 2, the sensitivity was always higher in specimen 2. The results are summarised in Table 7.

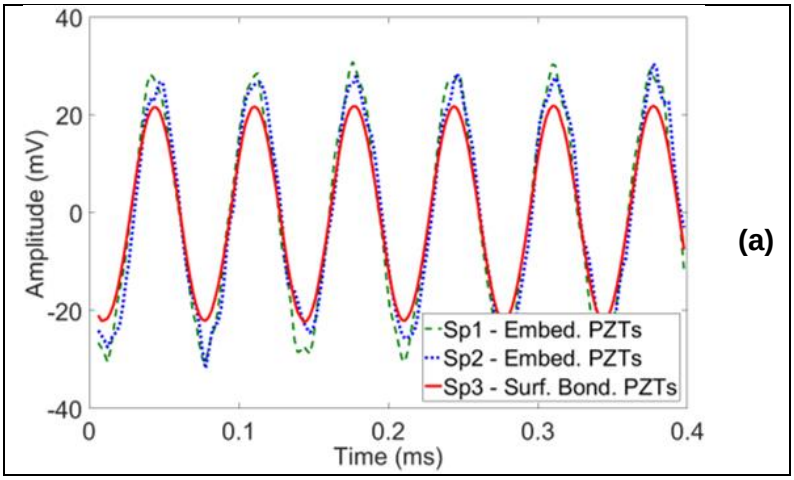

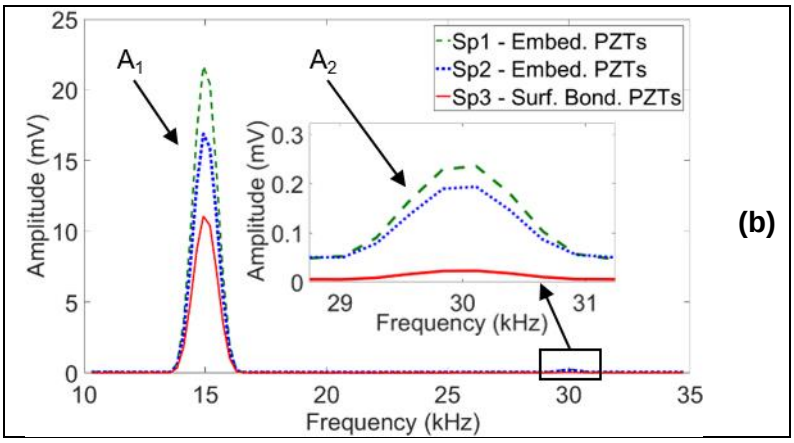

Figure 18: Amplitude of the received signal in time domain (a) and its associated spectrum (b) - case of 100V input signal at 15 kHz.

Table 7: Summary of results from NEWS experiment.

Input Signal	Specimen ID	A1 Amp. (mV)	A2 Amp. (mV)	Parameter $\|\beta\|$
75Vpp	1	15.733	0.209	0.00084
at	2	11.358	0.185	0.00143
15kHz	3	6.719	0.019	0.00042
87.5Vpp	1	18.485	0.226	0.00066
at	2	14.087	0.196	0.00099
15kHz	3	8.041	0.024	0.00038
100Vpp	1	23.786	0.235	0.00042
at	2	17.899	0.207	0.00065
15kHz	3	10.637	0.026	0.00023
112.5Vpp	1	27.626	0.243	0.00032
at	2	20.456	0.218	0.00052
15kHz	3	13.974	0.032	0.00016
125Vpp	1	30.961	0.259	0.00027
at	2	23.058	0.230	0.00043
15kHz	3	17.132	0.041	0.00014

5 CONCLUSIONS

In this paper a novel material processing technique for the electrical insulation of circular PZTs inserted between the plies of CFRP laminates was proposed. The top (conductive) surface of the embedded PZT was covered with a layer of E-glass fibre fabric. The effect of this embedding technique on the interlaminar properties of CFRP laminates was studied both numerically and experimentally, and it was compared with the effect of the conventional embedding technique using Kapton layers. Specifically, short-beam and long-beam three-point bending tests, and compression tests were

performed to determine the interlaminar shear strength, flexural strength and compressive strength of CFRP laminates with embedded PZTs and a layer of woven E-Glass fabric (G-specimens). Similarly, plain CFRP laminates (P-specimens) as well as CFRP laminates with embedded PZTs and a Kapton layer (K-specimens) were subject to the same tests. By analysing the results with a one-way ANOVA it was found that the mean values of compressive, flexural and interlaminar shear strength of G-specimens were all equal to those of P-specimens ($0.41 < p < 0.58$), suggesting that the proposed insulation technique had no impact on the mechanical properties of the CFRP laminates. The corresponding strength values in the case of K-specimens were all confirmed to be significantly lower ($0.0001 < p < 0.05$) than those of P-specimens. In addition, a comparative post-test fractographic analysis showed that the in bending tests, the mean damage size in G- and K-specimens was similar to the damage size in P-specimens ($0.37 < p < 0.87$). Only the damage opening in short-beam K-specimens was significantly bigger from that in P-specimens ($p = 0.03$). However, the remaining damage length and opening values were more similar between P-and G-specimens ($0.45 < p < 0.87$) than between P-and K-specimens ($0.37 < p < 0.79$). In compression tests, the brooming failure in P- and G-specimens was very similar suggesting that their behaviour under compressive loading was almost identical, whereas K-specimens failed by through-thickness shear followed by significant delamination at PZT plane. Finally, NEWS experiments on CFRP laminates with artificial in-plane delamination proved the effectiveness of glass fibre layers in protecting PZTs from being short-circuited, and also demonstrated the ability of detecting internal damage using embedded PZTs and nonlinear ultrasounds. The sensitivity of embedded PZTs in damage detection based on the effect of second harmonic generation was around two times higher than conventionally surface-bonded PZTs. In conclusion, this study can be considered as a contribution towards the development of composite materials with integrated sensing capabilities for ultrasonic SHM of aerospace structures. However, there are additional aspects to be studied in the future such as the effect of the proposed embedding technique on the fatigue endurance of composites and the ability of embedded arrays of PZTs with glass fibre layers to estimate the size and location of damage.

6 REFERENCES

[1] Masmoudi S, El Mahi A, Turki S, El Guerjouma R. Mechanical behavior and health monitoring by acoustic emission of unidirectional and cross-ply laminates integrated by piezoelectric implant. Applied Acoustics 2014;31(86):118-125.

[2] Konka HP. Characterization of composite piezoelectric materials for smart joint applications [Master's Thesis]. Louisiana (USA): Louisiana State University, 2010

[3] Birman V. Thermal effects on measurements of dynamic processes in composite structures using piezoelectric sensors. Smart materials and structures. 1996;5(4):379.

[4] Mall S, Coleman JM. Monotonic and fatigue loading behavior of quasi-isotropic graphite/epoxy laminate embedded with piezoelectric sensor. Smart Materials and Structures 1998;7(6):822-832.

[5] Paget CA, Levin K. Structural integrity of composites with embedded piezoelectric ceramic transducers. In: Symposium on Smart Structures and Materials. Int. Society for Optics and Photonics 1999; pp.306-313.

[6] Mall S. Integrity of graphite/epoxy laminate embedded with piezoelectric sensor/actuator under monotonic and fatigue loads. Smart Materials and Structures. 2002;11(4):527.

[7] Lin M, Chang FK. The manufacture of composite structures with a built-in network of piezoceramics. Composites Science and Technology 2002;62(7):919-939.

[8] Su Z, Wang X, Chen Z, Ye L, Wang D. A built-in active sensor network for health monitoring of composite structures. Smart Materials and Structures. 2006;15(6):1939.

[9] Arellano MT, Crouzeix L, Collombet F, Douchin B, Grunevald, YH. Mechanical characterization of an alternative technique to embed sensors in composite structures: the monitoring patch. Applied Composite Materials 2012;19(3-4):379-391.

[10] Tang HY, Winkelmann C, Lestari W, La Saponara V. Composite structural health monitoring through use of embedded PZT sensors. Journal of Intelligent Material Systems and Structures. 2011;22(8):739-55.

[11] Masmoudi S, El Mahi A, Turki S. Use of piezoelectric as acoustic emission sensor for in situ monitoring of composite structures. Composites Part B: Engineering. 2015;80(1):307-320.

[12] Wooh SC, Wei C. A high-fidelity ultrasonic pulse-echo scheme for detecting delaminations in composite laminates. Composites Part B: Engineering. 1999;30(5):433-441.

[13] Huang Y, Nemat-Nasser S. Structural integrity of composite laminates with embedded micro-sensors. In: Kara JP, editor. Sensor Systems and Networks: Phenomena, Technology, and Applications for NDE and Health Monitoring. SPIE, 2007.

[14] Clausen J, Specht U, Busse M, Lang A, Sanders J. Integration of glass fibre structures in aluminium cast parts for CFRP aluminium transition structures. Procedia Materials Science 2013;2:197-203.

[15] Boccardi S, Callá DB, Ciampa F, Meo M. Nonlinear elastic multi-path reciprocal method for damage localisation in composite materials. Ultrasonics. 2018;82(1):239-245.

[16] Ciampa F, Mankar A, Marini A. Phononic crystal waveguide transducers for nonlinear elastic wave sensing. Scientific Reports. 2017;7(1):14712.

[17] Scarselli G, Ciampa F, Nicassio F, Meo M. Non-linear methods based on ultrasonic waves to analyse disbonds in single lap joints. Proceedings of the Institution of Mechanical Engineers, Part C: Journal of Mechanical Engineering Science. 2017;231(16):3066-3076.

[18] Van Den Abeele KE, Sutin A, Carmeliet J, Johnson PA. Micro-damage diagnostics using nonlinear elastic wave spectroscopy (NEWS). NDT & E International. 2001;34(4):239-248.

[19] Sohn H, Park G, Wait JR, Limback NP, Farrar, CR. Wavelet-based active sensing for delamination detection in composite structures. Smart Materials and structures 2003;13(1):153.
[20] Polimeno U, Meo M, Almond DP, Angioni, SL. Detecting low velocity impact damage in composite plate using nonlinear acoustic/ultrasound methods. Applied Composite Materials 2010;17(5):481-488.
[21] Ricci F, Mal AK, Monaco E, Maio L, Boffa ND, Di Palma M, Lecce L. Guided waves in layered plate with delaminations. In: EWSHM-7th European Workshop on Structural Health Monitoring. Nantes, July, 2014.
[22] Ciampa F, Pickering S, Scarselli G, Meo M. Nonlinear damage detection in composite structures using bispectral analysis. In: SPIE Smart Structures and Materials+ Nondestructive Evaluation and Health Monitoring. Int. Society for Optics and Photonics. San Diego, March, 2014.
[23] Ciampa F, Scarselli G, Meo M. On the generation of nonlinear damage resonance intermodulation for elastic wave spectroscopy. The Journal of the Acoustical Society of America 2017;141(4):2364-2374.
[24] Meo M, Zumpano G. Nonlinear elastic wave spectroscopy identification of impact damage on a sandwich plate. Composite structures 2005;71(3):469-474
[25] Landau LD, Lifshitz EM. Theory of Elasticity. Oxford: Pergamon, 1986; p.476
[26] Zagrai A, Donskoy D, Chudnovsky A, Golovin E. Micro-and macroscale damage detection using the nonlinear acoustic vibro-modulation technique. Research in Nondestructive Evaluation 2008;19(2):104-128.
[27] Zaitsev V, Sas P. Nonlinear response of a weakly damaged metal sample: a dissipative modulation mechanism of vibro-acoustic interaction. J. Vib. Control 2000;6:803–822.
[28] Buck O, Morris WL, Richardson JM. Acoustic harmonic generation at unbonded interfaces and fatigue cracks. Applied Physics Letters 1978;33(5):371-372.
[29] Antonets VA, Donskoy DM, Sutin AM. Nonlinear vibro-diagnostics of flaws in multilayered structures. Mechanics of Composite Materials. 1986;15:934-937.
[30] Hirsekorn S, Delsanto PP. On the universality of nonclassical nonlinear phenomena and their classification. Applied Physics Letters 2004;84(8):1413-1415.
[31] Solodov I, Bai J, Bekgulyan S, Busse G. A local defect resonance to enhance acoustic wave-defect interaction in ultrasonic nondestructive evaluation. Applied Physics Letters 2011; 99(21):211911.
[32] Solodov I. Resonant acoustic nonlinearity of defects for highly-efficient nonlinear NDE. Journal of Nondestructive Evaluation 2014;33(2):252-262.
[33] Dragan K, Dziendzikowski M, Kurnyta A, Leski A, Bienias J. Structural health monitoring of composite structures with use of embedded PZT piezoelectric sensors. In: ECCM-16th European Conference on Composite Materials. Seville, June, 2014.
[34] BS Standard EN ISO 14130:1997. Fibre-reinforced plastic composites - Determination of apparent interlaminar shear strength by short-beam method. British Standards Institute, 1997.
[35] Moulin E, Assaad J, Delebarre C, Kaczmarek H, Balageas D. Piezoelectric transducer embedded in a composite plate: application to Lamb wave generation. Journal of Applied Physics. 1997;82(5):2049-2055.
[36] Shin DK, Kim HC, Lee JJ. Numerical analysis of the damage behavior of an aluminium/CFRP hybrid beam under three point bending. Composites Part B: Engineering 2014;31(56):397-407.
[37] Giddings PF, Bowen CR, Salo AI, Kim HA, Ive A. Bistable composite laminates: effects of laminate composition on cured shape and response to thermal load. Composite Structures 2010;92(9):2220-2225.

[38] Phadnis VA, Pandya KS, Naik NK, Roy A, Silberschmidt VV. Ballistic impact behaviour of woven fabric composite: Finite element analysis and experiments. In: Journal of Physics: Conference Series. IOP Publishing 2013;451(1):012019.
[39] Zako M, Uetsuji Y, Kurashiki T. Finite element analysis of damaged woven fabric composite materials. Composites Science and Technology 2003;63(3):507-516.
[40] Physik Instrumente (PI) GmbH & Co. Piezoelectric Actuators. PICeramic.com [Online Datasheet] 2012. Available at: http://fisica.cab.cnea.gov.ar/bt/images/d/d3/PICat.pdf.
[41] Hyer MW. Stress analysis of fiber-reinforced composite materials. Singapore: McGraw-Hill International, 1998; pp.26.
[42] Willis BM. Applying finite element analysis with a focus on tensile damage modeling of carbon fiber reinforced polymer laminates [Master's Thesis]. Ohio (USA): Ohio State University, 2013; pp.30-33
[43] Shi, Y., Swait, T., & Soutis, C. Modelling damage evolution in composite laminates subjected to low velocity impact. Composite Structures, 94(9), 2902-2913, 2012.
[44] ASTM Standard D7264/D7264-07. Standard test method for flexural properties of polymer matrix composite materials. ASTM International, 2007.
[45] BS Standard EN ISO 14126:1999. Fibre-reinforced plastic composites - Determination of compressive properties in the in-plane direction. British Standards Institute, 1999.
[46] Daniel WW. Biostatistics: a foundation for analysis in the health sciences. New York: John Wiley and Sons, 1999; chapter 8.
[47] Pezzullo J. Biostatistics for dummies. New Jersey: John Wiley & Sons, 2013; p.164.
[48] Hogg RV, Ledolter J. Engineering statistics. Macmillan Pub Co, 1987.